

Line Profiles of Intermediate Redshift Type Ia Supernovae ¹

Kohki Konishi^{2,3}, Joshua A. Frieman^{4,5,6}, Ariel Goobar^{7,8}, John Marriner⁴, Jacob Nordin^{7,8},
Linda Östman⁹, Masao Sako¹⁰, Donald P. Schneider¹¹, Naoki Yasuda^{2,12}

kohki@icrr.u-tokyo.ac.jp

ABSTRACT

We present the temporal evolution of line profiles ranging from near ultraviolet to optical wavelengths by analyzing 59 Subaru telescope spectra of normal Type Ia Supernovae (SNe Ia) in the intermediate redshift range ($0.05 < z < 0.4$) discovered by the Sloan Digital Sky Survey-II (SDSS-II) Supernova Survey. We derive line velocities, peak wavelengths and pseudo-equivalent widths (pEWs) of these lines. Additionally, we compare the line profiles around the date of

Department of Physics, Stockholm University, 106 91 Stockholm, Sweden.

Oskar Klein Centre for Cosmo Particle Physics, AlbaNova, 106 91 Stockholm, Sweden.

¹Based in part on data collected at Subaru Telescope, which is operated by the National Astronomical Observatory of Japan.

²Department of Physics, Graduate School of Science, University of Tokyo, Tokyo 113-0033, Japan.

³Institute for Cosmic Ray Research, University of Tokyo, Kashiwa 277-8582, Japan.

⁴Center for Particle Astrophysics, Fermi National Accelerator Laboratory, P.O. Box 500, Batavia, IL 60510, USA

⁵Kavli Institute for Cosmological Physics, The University of Chicago, 5640 South Ellis Avenue Chicago, IL, 60637, USA

⁶Department of Astronomy and Astrophysics, The University of Chicago, 5640 South Ellis Avenue Chicago, IL, 60637, USA

⁷Department of Physics, Stockholm University, 106 91 Stockholm, Sweden.

⁸Oskar Klein Centre for Cosmo Particle Physics, AlbaNova University Center, 106 91 Stockholm, Sweden.

⁹Institut de Física d'Altes Energies, Universitat Autònoma de Barcelona, Bellaterra, Spain.

¹⁰Department of Physics and Astronomy, University of Pennsylvania, Philadelphia, PA 19104, USA.

¹¹Department of Astronomy and Astrophysics, Pennsylvania State University, University Park, PA 16802 USA.

¹²Institute for the Physics and Mathematics of the Universe, University of Tokyo, Kashiwa 277-8582, Japan.

maximum brightness with those from their nearby counterparts. We find that line profiles represented by their velocities and pEWs for intermediate redshift SNe Ia are consistent with their nearby counterparts within 2σ . These findings support the picture that SNe Ia are a “standard” candle for the intermediate redshift range as has been shown between SNe Ia at nearby and high redshifts. There is a hint that the “Mg II λ 4300” pEW distribution for intermediate redshift SNe Ia is larger than for the nearby sample, which could be interpreted as a difference in the progenitor abundance.

Subject headings: cosmology: observations - line: profiles - supernovae: general - surveys

1. Introduction

The diversity of type Ia supernovae (SNe Ia) has been extensively investigated over the past thirty years; see Branch et al. (1981, 1988); Wells et al. (1994) for initial studies. Photometric lightcurves have revealed that the maximum luminosity is related to the decline rate of luminosity. A parameter for SN lightcurve variations, Δm_{15} , is defined as the magnitude decline between the maximum brightness date and 15 days later. SNe Ia are found to be brighter with smaller values of Δm_{15} (e.g. Phillips et al. 1999). The maximum luminosity is also related to (B-V) color (e.g. Riess, Press & Kirshner 1996; Tripp 1998). These relations play an essential role in the standardization of maximum luminosity and therefore the description of the accelerating universe (Riess et al. 1998; Perlmutter et al. 1999). Spectra are also suited for the investigation of SN Ia diversity, since they can retain subtle information which would be blurred in photometry: chemical composition and excitation levels of ejected materials such as magnesium, silicon, sulfur, calcium, titanium, chromium and iron.

The spectroscopic diversity of SNe Ia is seen in many features. The large velocity scatter ($\sim 3,000$ km sec $^{-1}$) of the location of the “Si II λ 6355” line has been presented in Branch et al. (1988). The temporal evolution of various optical lines is examined in Folatelli (2004): equivalent widths (pEWs) of the “Fe II λ 4800” feature evolve in a homogeneous way with phase, irrespective of their lightcurves. The “Mg II λ 4300” pEW, however, increases abruptly at later times for SNe Ia with smaller Δm_{15} . The temporal evolution of “Si II λ 4130”, “Si II λ 5972” and “Si II λ 6355” pEWs were also found to be heterogeneous.

The chemical composition of SN progenitors is supposed to have an important impact on the appearance of spectral features. Lentz et al. (2000) examined metallicity effects of progenitors on SN spectra at several phases with simulations, by scaling all elements

heavier than oxygen in the unburned carbon/oxygen (CO) layer. UV features are shown to move blueward with higher metallicity. Since metallicity evolves with redshift (Rodrigues et al. 2008), SN spectral features would be expected to change over cosmic time and perhaps bias the cosmological parameter measurements. Coil et al. (2000) examined two spectra of SNe Ia at high redshift (high- z) and reported no significant difference from nearby SNe Ia. Blondin et al. (2006) compared SN Ia spectra taken for the Equation of State: Super-Novae trace Cosmic Expansion survey (ESSENCE; Miknaitis et al. 2007) with nearby SN Ia spectra in the SUPERNOVA SPECTRA(SUSPECT) database¹. They measured line velocities of “Ca II λ 3945”, “Si II λ 5454”, “Si II λ 5640” and “Si II λ 6355” for nearby and high- z ($0.3 \lesssim z \lesssim 0.7$) SNe Ia to examine the temporal evolution of line velocities. This work, and that of Garavini et al. (2007), found no evolution between nearby and high- z SNe Ia.

A possible redshift-dependence in the temporal evolution of features has been reported recently. Around half of the SN Ia spectra at high- z ($z \sim 0.7$) taken for the SuperNova Legacy Survey (SNLS; Astier et al. 2006) show lower “Mg II λ 4300” pEWs than the 1σ pEW distribution of their nearby counterparts at 5 to 10 days after the dates of maximum brightness (Bronder et al. 2008). The observed differences might be caused by selection effects in the high- z sample: the abrupt increase in “Mg II λ 4300” occurs later in the brighter supernovae that tend to be selected for spectroscopic follow-up, especially at high- z . A decrease of the “Fe II λ 4800” pEW was reported by creating four composite spectra in the redshift range of 0.1 to 0.8. The redshift evolution was further investigated by constructing composite spectra of nearby, SNLS/Keck, and Hubble Space Telescope (HST) reference samples (Sullivan et al. 2009). They claimed a lower intermediate mass element (IME) abundance toward $z \lesssim 1$ by showing the drop of average pEW for “Ca II λ 3945”, “Si II λ 4130”, and “Mg II λ 4300”. The extent of SN Ia diversity and their possible evolution is still uncertain. While SNe Ia spectra in the nearby and high- z ranges have often been obtained, few SNe Ia spectra in the intermediate redshift range have been observed.

The Sloan Digital Sky Survey-II (SDSS-II) Supernova Survey (Frieman et al. 2008; Sako et al. 2008) has obtained over 500 spectroscopically confirmed SNe Ia in the intermediate redshift range. Lightcurves and spectra of the first year sample are described in Holtzman et al. (2008) and Zheng et al. (2008). A subset of SDSS-II SN Ia spectra by the New Technology Telescope and the Nordic Optical Telescope (NTT/NOT) was used for an optical spectral feature study (Östman et al. 2011; Nordin et al. 2011). We investigate near UV to optical line profiles of SNe Ia obtained by a different reduction pipeline, galaxy subtraction method, and selection criteria (Konishi et al. 2011a) by comparing a sample of nearby SN

¹<http://bruford.nhn.ou.edu/~suspect/>

Ia spectra with those obtained by the Subaru telescope in the course of the SDSS SN survey. The following is the outline of this paper. The data are summarized in §2. §3 gives the measurement methods of spectral features. The temporal and redshift evolution of these features are presented in §4. We discuss and conclude this paper in §5 and §6.

2. Data

2.1. Intermediate redshift Supernovae

An extension of the Sloan Digital Sky Survey (York et al. 2000), the SDSS-II Supernova Survey, obtained lightcurves of hundreds of SNe Ia at the intermediate redshift, $0.05 < z < 0.40$ (Frieman et al. 2008; Sako et al. 2008; Holtzman et al. 2008). The SN survey have acquired observations from September to November during 2005 - 2007 on the 300 square degrees of the equatorial region (Stripe 82; Stoughton et al. 2002). The SDSS 2.5m telescope (Gunn et al. 2006) and camera (Gunn et al. 1998) have been used with *ugriz* filters (Fukugita et al. 1996) to repeatedly scan the wide field of sky. Spectroscopy for SN identification and redshift determination was performed with various telescopes including the Subaru telescope (Konishi et al. 2011a); see also Sako et al. (2008); Zheng et al. (2008); Östman et al. (2011); Foley et al. (2010).

We observed 62 SN Ia spectra with the Faint Object Camera and Spectrograph (FOCAS; Kashikawa et al. (2002)) mounted on the Subaru telescope during 2005 and 2006. The instrumental wavelength range was 3600 Å (4000 Å for Year 2005) to 6000 Å for blue side spectra and 5000 Å to 9000 Å for red side spectra at a spectral resolution of 500. We generally took blue and then red side spectra for each SN and combined them using flux densities at overlapping wavelengths. SN observations were not typically made at the parallactic angle, but the atmospheric refraction was corrected by an atmospheric dispersion corrector. Phases of SN Ia spectra, elapsed rest-frame days from the maximum date (p), are determined by the SALT2 lightcurve fitter (Guy et al. 2007). Lightcurve parameters of lightcurve width x_1 and color c_{salt} are also determined (Konishi et al. 2011a). Each of intermediate redshift SNe Ia sample is determined as *gold* or *silver* SNe using the following photometric and spectroscopic criteria.

Lightcurves: Since the season for photometric observations was limited, some lightcurves do not have sufficient phase coverage to accurately determine photometric properties. We set the following criteria for their lightcurves:

1. at least one data point with $p < -4$.

2. at least one data point with $p > +4$.
3. at least five data points with $-20 < p < +60$.
4. lightcurve parameters with $|x_1| < 5.0$ and/or $|c_{salt}| < 2.0$, which are the SALT2 limits of these parameters.

The criteria for lightcurves are similar to those for the cosmology sample (Kessler et al. 2009a) except that our requirement for the date of first observation is slightly more stringent to securely determine the dates of maximum luminosity.

Spectra: The observed SN spectra generally also contained light from host galaxy. In order to examine line velocities and pEWs precisely, SN spectra were extracted from 2 Dimensional (2D) galaxy-contaminated spectra by fitting each spatial profile with point and broad components without the aid of galaxy template spectra (Konishi et al. 2011a). This method is similar to that of Blondin et al. (2005); Baumont et al. (2008). The 2D extraction method worked well for most of our intermediate redshift spectra but failed when the bestfit width for a SN component was incompatible with the seeing size, which can arise if a SN was located too near the center of its host galaxy. We set the following criteria for spectral extraction:

1. the separation of the SN and the host center was larger than 1 pixel (0.312 arcsec) or there was no apparent host
2. a bimodal spatial profile was found: a minimum appeared in the signal between the SN and its host center.

Table 1 summarizes normal intermediate redshift SNe Ia observed by the Subaru telescope. The SDSS internal identification number (ID) and the IAU name are written in Columns 1 and 2. The Galaxy extinction from Schlegel, Finkbeiner & Davis (1998) is listed in Column 3. The time of each observation is in Column 4. The redshift and the method to obtain the redshift are shown in Column 5: “ge” indicates that the redshift of the target was determined from galaxy emission line(s), “ga” from galaxy absorption line(s) and “sn” from fitting the SN spectrum. For more details about the redshift determination see Konishi et al. (2011a). Column 6 is the validity of the data. We regard those SNe Ia which passed all of the lightcurve and spectra criteria as the *gold* sample, which is indicated as “G” in Column 6. If a SN Ia fails at least one of the lightcurve (spectral) criteria, it is regarded as photometrically *silver* (spectroscopically *silver*), which is indicated as “PS (SS)” *silver*. Those which failed both photometric and spectroscopic criteria are indicated as “S” in Column 6. A total of 38 SNe Ia are regarded as *gold* and 21 as *silver*. Of the 21 *silver* sample,

10 are photometrically classified as *silver*, another 9 are spectroscopically classified, and the other 2 are both. SNe Ia classified as *silver* by the fourth lightcurve criterion are SN2006jf and SN2006jv and those by the second spectral criterion are SN2005hz, 2006qa and 2006qe. Column 7 contains the phase of the SN Ia spectra. Only one SN Ia spectrum was observed for each object in our sample. The distributions of phase, redshift, lightcurve width x_1 , and color c_{salt} for 59 intermediate redshift SNe Ia (dotted) and 38 *gold* SNe Ia (solid) are shown in Figure 1. The Subaru sample is smaller (59 versus 141 SNe Ia) than the NTT/NOT sample (Östman et al. 2011; Nordin et al. 2011) but higher redshift (0.25 ± 0.08 versus 0.17 ± 0.07).

2.2. Control sample

We use two types of nearby normal SNe Ia datasets for comparison of line features with the intermediate redshift sample. Here we call SNe Ia except for 1991bg-like, 1991T-like and peculiar (in any sense) objects as normal ones. One consists of optical spectra (**Opt**) and the other of UV spectra (**UV**).

The **Opt** sample consists of 121 spectra at $-10 < p < +40$ from 12 well-observed SNe Ia. This sample is the same sample examined by Bronder et al. (2008) except that the sample lacks SN1991T-like, SN1991bg-like and unpublished samples. We downloaded spectra from the SUSPECT database and removed the atmospheric A line (absorption at 7600 Å) from them if we found it near 7600 Å in their observed frame. The **UV** sample consists of 20 spectra at $-10 < p < +10$ from 8 SNe Ia. We use the public spectral dataset obtained with the International Ultraviolet Explorer and the HST (Foley, Filippenko & Jha 2008b) and chose spectra in the wavelength region from 3050 to 3250 Å from the dataset. SN1991bg-like or SN1991T-like samples were not included. Rest frame *BVR*-band lightcurves are comparable to *gri* bands for the intermediate redshift SNe Ia. Lightcurves were gathered from various papers (Buta & Turner 1983; Ciatti et al. 1988; Buta, Corwin & Opal 1985; Phillips et al. 1987; Hamuy et al. 1991; Ford et al. 1993; Leibungut et al. 1993; Wells et al. 1994; Lira et al. 1998; Jha et al. 1999; Riess et al. 1999; Krisciunas et al. 2001, 2003, 2004; Valentini et al. 2003; Krisciunas et al. 2004; Altavilla et al. 2004; Anupama et al. 2005; Riess et al. 2005). A *B*-band lightcurve for SN1991M and *R*-band lightcurves for SN1982B, SN1986G and SN2001ba were missing. The maximum date and other lightcurve parameters for the **Opt** and **UV** samples were obtained using the SALT2 (Guy et al. 2007) code as for the intermediate redshift sample. Figure 2 shows distributions of spectral phases (upper left), redshift (upper right), lightcurve width x_1 (lower left) and color c_{salt} (lower right) for the nearby sample of **Opt** (red) and **UV** (blue) together with the intermediate redshift *gold* SNe Ia (black).

Tables 2 and 3 summarize the details of the **Opt** and **UV** spectra, respectively. Column 1 is the IAU name for each SN. SN coordinates are shown in Columns 2 and 3. Column 4 is the Galactic color excess $E(B-V)$ from the Schlegel, Finkbeiner & Davis (1998) reddening map and Column 5 is the redshift. Redshifts were corrected using the NASA/IPAC Extragalactic Database (NED)². The Galactic extinction was corrected using the Cardelli, Clayton & Mathis (1989) law and $E(B-V)$ values.

Additionally, we used the SN Ia spectral template of Hsiao et al. (2007). This template was constructed from a stack of observed spectra. Since this template covers the UV-to-optical wavelength region during $-10 < p < +40$, we used it to estimate the mean and dispersion of nearby and intermediate redshift SNe Ia (§4.2).

3. Measurements

The definition of Folatelli (2004) for each absorption feature is adopted (Figure 3). Note that this convention can cause some confusion. Some observed lines (e.g. “Si II λ 4130”) are a mixture of several lines from different elements, which can vary with time, temperature, and abundances (Branch et al. 2008). We measured line velocities and pEWs for “Ca II λ 3945” (feature 1), “Mg II λ 4300” (feature 3), “Fe II λ 4800” (feature 4), and “Si II λ 6355” (feature 7) from spectra in the range $-10 < p < +40$, but we only measured these quantities for “Si II λ 4130” (feature 2), “Si II λ 5454,5640” (feature 5) and “Si II λ 5972” (feature 6) from spectra in the range $-10 < p < +10$ when those features are most pronounced. We also measured the wavelength for the “UV2” feature, locating between the absorption lines of Mg II and Fe II at ~ 3200 Å (e.g. Weiler et al. 2003).

3.1. Spectrum smoothing

Since line forming regions are expanding, spectral features are intrinsically broadened and noisy spectra can be smoothed in order that as little intrinsic information is missed as possible. We smoothed intermediate redshift spectra $f_{obs}(\lambda)$ by using their uncertainty $f_{err}(\lambda)$: each point in the spectrum is weighted according to the value of its inverse variance. A smoothed spectrum $\bar{f}(\lambda)$ is obtained as

$$\bar{f}(\lambda) = \frac{\sum_{\lambda'} W(\lambda, \lambda') f_{obs}(\lambda')}{\sum_{\lambda'} W(\lambda, \lambda')}, \quad (1)$$

²<http://nedwww.ipac.caltech.edu/>

where the weight $W(\lambda, \lambda')$ is

$$W(\lambda, \lambda') = \frac{G(\lambda, \lambda', \sigma_G)}{f_{err}(\lambda')} \quad (2)$$

$$G(\lambda, \lambda', \sigma_G) = \frac{1}{\sqrt{2\pi}} \exp\left(-\left(\frac{\lambda - \lambda'}{\sigma_G}\right)^2\right). \quad (3)$$

This procedure given in Blondin et al. (2006) is based on the intrinsic broadening of SN features due to large expansion velocities their in line forming regions, and takes into account flux uncertainties which depend on wavelengths. Assuming the velocity of this broadening to be $1500 - 3000 \text{ km sec}^{-1}$, one can write a smoothing factor $\sigma_G = (v/c)\lambda$. We set $v = 1500 \text{ km sec}^{-1}$ for optical wavelengths and $v = 3000 \text{ km sec}^{-1}$ for UV wavelengths. This relatively larger velocity avoids misidentification of the “UV2” peak wavelength from several spikes which probably result from high-frequency noises.

Figure 4 is an example of the result of this convolution. The black line is the observed spectrum, and the red line the smoothed spectrum. Since absorption features are determined more clearly in a smoothed spectrum than in its noisy spectrum, we use smoothed spectra for the measurements of line velocities and pEW.

3.2. Line velocity measurements

A line velocity v_{abs} is determined by using the relativistic Doppler formula.

$$v_{abs} = \frac{(\lambda_{obs}/\lambda_{rest})^2 - 1}{(\lambda_{obs}/\lambda_{rest})^2 + 1} c, \quad (4)$$

where λ_{obs} is the wavelength of an absorption minimum. The smoothed flux at the wavelength takes its minimum within the wavelength region for the feature. The vertical arrow in Figure 4 is an example of the absorption minimum. The wavelength regions and representative wavelengths of all the features are summarized in Columns 3 and 5 of Table 4. Although a “Ca II $\lambda 3945$ ” feature sometimes shows a ‘W’ shape due to the additional contribution of the “Si II $\lambda 3858$ ” line, we assumed that the largest contribution to this absorption is “Ca II $\lambda 3945$ ”, and measured the wavelengths of the deepest absorption minimum for “Ca II $\lambda 3945$ ”.

Since an absorption minimum of a P Cygni profile is shifted blueward, absorption line velocities are negative. Following Blondin et al. (2006), we use the words *increase* and *decrease* literally, e.g. the velocity increases from $-10,000 \text{ km sec}^{-1}$ to $-9,000 \text{ km sec}^{-1}$, and decreases from $-10,000 \text{ km sec}^{-1}$ to $-15,000 \text{ km sec}^{-1}$.

3.3. Pseudo-equivalent width measurements

A “pseudo” EW (pEW) of an absorption feature is defined to be an EW for a pseudo-continuum (Garavini et al. 2007; Bronder et al. 2008; Foley et al. 2008a; Sullivan et al. 2009). The pseudo-continuum is often assumed to change linearly, as shown in the green line in Figure 4, between two spectral peaks of the features next to the absorption (we call these peaks “absorption boundaries”). The pEW is determined as follows:

$$pEW = \sum_{i_w=1}^N \left(1 - \frac{f_{obs}(\lambda_{i_w})}{f_c(\lambda_{i_w})} \right) \Delta\lambda_{i_w}, \quad (5)$$

where N is the number of wavelength pixels underneath the pseudo-continuum f_c . The wavelengths of the two absorption boundaries (λ_1 and λ_N) are determined from the smoothed spectrum f_{obs} by searching for peak fluxes within the wavelength regions in Column 4 of Table 4. $\Delta\lambda_{i_w}$ is the wavelength interval between neighboring wavelengths.

Uncertainty estimation for line velocities and pEWs: We measure wavelengths of absorption minima, a bump peak and absorption boundaries from smoothed spectra. Although the intrinsic broadenings of 3,000 km sec^{−1} or 1,500 km sec^{−1} are typical, this process might bias the wavelengths. We estimate the uncertainty in the line measurements using a Monte Carlo simulation. There is a “blank” region in 2D spectra which was far from the SN and far from the galaxy, so that only background light was reaching the detector. We compute the flux error $f_{err}(\lambda)$ from the sky background of the actual spectrum added in quadrature to the photon counting errors of the smoothed spectrum. The simulated spectrum is the actual smoothed spectrum smeared by the computed error. This procedure is repeated 100 times to derive the average and standard deviation of absorption minimum wavelength or pEWs. Uncertainties on the line velocities are set to the velocity corresponding to the standard deviation of the measured absorption minima. The statistical errors for the **Opt** sample are negligible. We use a typical galaxy rotational speed (200 km sec^{−1}) for the velocity error and assign no error for the pEW measurements.

4. Spectral features

4.1. Temporal evolution

The signal-to-noise ratio (S/N) range for most of the intermediate redshift SN Ia spectra is from 3 to 10 per 2 Å (Konishi et al. 2011a). Typical SN Ia features are easy to recognize by visual inspection. We show the temporal evolution measurements of line velocities and pEWs.

Line velocities: Blondin et al. (2006) measured line velocities of “Ca II λ 3945”, “Si II λ 5454”, “Si II λ 5640” and “Si II λ 6355” for 36 high- z SNe Ia discovered by the ESSENCE survey. The temporal evolution of line velocities for the high- z sample was reported to be consistent with those for the nearby sample. Ellis et al. (2008) measured line velocities of “UV2” and “Si II λ 4130” for 36 high- z SNe Ia from the SNLS/Keck sample to examine the behavior of UV features compared to an optical line.

In Figure 5, we plot the temporal evolution of line velocities for six features of nearby and intermediate redshift SNe Ia: (a) “Ca II λ 3945”, (b) “Si II λ 4130”, (c) “Si II λ 5454”, (d) “Si II λ 5640”, (e) “Si II λ 5972”, and (f) “Si II λ 6355”. intermediate redshift SNe Ia are shown as circles (filled for *gold* SNe Ia and open for *silver* SNe Ia) and the nearby sample as black pluses. As has been found previously in nearby and high- z SNe Ia (e.g. Blondin et al. 2006), one can see the following for the intermediate redshift SNe Ia: (i) the range of line velocities for the “Ca II λ 3945” line is wide, from $-20,000 \text{ km sec}^{-1}$ to $-10,000 \text{ km sec}^{-1}$ at $-7 \lesssim p \lesssim 0$. This range converges to a few $\times 10^3 \text{ km sec}^{-1}$ at $p \sim 30$. (ii) The “Si II λ 4130” line velocity is almost constant at $-11,000 \text{ km sec}^{-1}$ for $-7 \lesssim p \lesssim 0$ and smoothly increases by $\sim 3,000 \text{ km sec}^{-1}$ to $p = 5$. (iii) The velocity for the “Si II λ 5454” line is $-10,000 \text{ km sec}^{-1}$ at $-7 \lesssim p \lesssim -3$ and increases only gradually to $-7,000 \text{ km sec}^{-1}$ at $-7 \lesssim p \lesssim -3$. (iv) The “Si II λ 5640” line velocity is $-11,000 \text{ km sec}^{-1}$ at $-7 \lesssim p \lesssim -3$ and gradually increases to $-9,000 \text{ km sec}^{-1}$ afterwards. (v) The “Si II λ 5454” velocity is always larger than the “Si II λ 5640” velocity at a fixed phase. Branch et al. (2008) explains this increase as the contamination of iron peak elements, and the “Si II λ 5454” line becomes undetectable at $p \sim 10$. (vi) The “Si II λ 5972” line velocity is constant around $-10,000 \text{ km sec}^{-1}$ at $-7 \lesssim p \lesssim +3$ and slightly decreases afterwards. Branch et al. (2005) explains this increase as the strengthening of the NaI D line. (vii) The “Si II λ 6355” line velocity is constant around $-11,000 \text{ km sec}^{-1}$ for $-7 \lesssim p \lesssim -3$ and increases by a few $\times 10^3 \text{ km sec}^{-1}$ until $p \sim 10$. Several measurements of SN1998bu show large negative velocities at $30 < p < 40$. Branch et al. (2008) explains the velocity decrease at $30 \lesssim p$ as the inclusion of Fe II. Typical velocities for Ca, Si and S are $-15,000 \text{ km sec}^{-1}$, $-10,000 \text{ km sec}^{-1}$ and $-9,000 \text{ km sec}^{-1}$ at maximum brightness (Figure 5), which confirms an onion-like structure of the SN interior³.

In Figure 6, we show the peak wavelength of the “UV2” bump against SN phases for the intermediate redshift and **UV** sample (the same labels as in Figure 5). The “UV2” wavelength for intermediate redshift *gold* SNe Ia ranges from 3100 to 3200 Å throughout the range of phases of the observations.

Pseudo-equivalent widths: Garavini et al. (2007) measured “Ca II λ 3945”, “Mg II λ 4300”

³Elements with large negative velocity are distributed in outer layers.

and “Fe II λ 4800” pEWs for 12 SNe Ia ($0.2 < z < 0.9$) discovered by the SCP and reported a consistency between the temporal evolutions of pEWs for nearby and high- z SNe Ia. Bronder et al. (2008) measured “Ca II λ 3945”, “Si II λ 4130” and “Mg II λ 4300” for 46 SNLS/Gemini SNe Ia and found a marginal difference only for the “Mg II λ 4300” feature. This study contains more features than these previous studies.

In Figure 7, we plot the temporal evolution of pEWs for all the measured lines of nearby and intermediate redshift SNe Ia (the same labels as Figure 5): (a) “Ca II λ 3945”, (b) “Si II λ 4130”, (c) “Mg II λ 4300”, (d) “Fe II λ 4800”, (e) “S II W”, (f) “Si II λ 5972” and (g) “Si II λ 6355”. One can see the following: (i) The “Ca II λ 3945” pEW is 120 Å at $p \sim 0$ and decreases by 50 Å to $p \sim 10$. (ii) The “Si II λ 4130” pEW stays nearly constant around 10 Å at $p < 0$ and increases only gradually until $p \sim 7$. (iii) The “Mg II λ 4300” pEW is around 100 Å at $p < 7$ and increases toward later phases. Two SDSS SNe Ia (SN12883 and SN12972) have a particularly small “Mg II λ 4300” pEWs at $p \sim 10$. (iv) The “Fe II λ 4800” pEW is around 100 Å at $-5 < p < 0$ and it increases monotonically with SN phase to 400 Å at $p \sim 30$. Fe II is the element which dominates optical spectra as spectra evolve temporally (Branch et al. 2005). (v) The “S II W” pEW is large (80 Å) until $p = 3$ and then begins to decrease. This feature is only visible until $p < 10$. Branch et al. (2005) explains that Fe II lines give a larger contribution to this feature at later phases. The temporal evolution for this feature has been displayed for the first time. (vi) The “Si II λ 5972” pEW is 10 Å at $p \sim -10$ and increases monotonically. The “Si II λ 5972” feature is increasingly contaminated, again, mainly by Na I D, which dominates at $p \sim 10$. (vii) The “Si II λ 6355” pEW is 90 Å at $p \sim 0$ with the range of 30 Å. It becomes large (200 Å) at $p \sim 30$. This is attributed to an iron feature (Branch et al. 2008).

Overplotted are high- z SNe Ia from Blondin et al. (2006) (cyan pluses) and Ellis et al. (2008) (green pluses) for velocities (Figure 5). High- z SNe Ia from Garavini et al. (2007) are in blue and those from Bronder et al. (2008) in green for pEWs (Figure 7). Since their spectra are not available to the public, we use values determined by these studies and averaged in the same manner as our sample. For the UV2 line, high- z SNe Ia from Ellis et al. (2008) are in green pluses and theoretical predictions of Lentz et al. (2000) with the metallicities in the un-burned outer layer of 0.1, 0.3, 1.0 to 3.0 solar are in gray lines (from top to bottom, Figure 6). The measurements for the Hsiao et al. (2007) template are shown with a solid line. The dispersions of the “UV2” wavelength for nearby and intermediate redshift SNe Ia (32 Å) were larger than what can be explained by the variation of the progenitor metallicity. Different sets of data are qualitatively compared in §4.2.

4.2. Redshift evolution

Bronder et al. (2008) examined the redshift dependences of the velocity for “Ca II λ 3945” and the pEWs for “Ca II λ 3945”, “Si II λ 4130” and “Mg II λ 4300” within their high- z SNe Ia and showed that no systematic evolution of SN Ia properties were seen within the redshift ranges for SNLS SNe Ia. Foley et al. (2008a) made ESSENCE SN Ia composite spectra for $0 < z < 0.6$ and measured “Ca II λ 3945”, “Si II λ 4130”, and “Fe II λ 4800” pEWs for these composites. They reported that the average “Fe II λ 4800” pEW is lower for higher SNe Ia composites, possibly due to the larger number of bright and hot SNe Ia in the high- z sample (but they also mention that this can not explain all the observed absorption profiles). Sullivan et al. (2009) also constructed composites to report smaller average pEWs for “Ca II λ 3945”, “Si II λ 4130” and “Mg II λ 4300” with increasing redshifts. These effects are interpreted as the changing demographics of SNe Ia by these authors, that is a larger fraction of “prompt (Mannucci, Della Valle & Panagia 2006)” SNe Ia at higher redshifts (Howell et al. 2007). Nordin et al. (2011) reported no signs of velocity differences in their sample and nearby counterparts, but found a fraction ($\sim 20\%$) of SNe Ia with lower pEWs than nearby averages, which was interpreted as partly caused by slightly peculiar SNe Ia (like e.g. the Shallow Silicon subtype, (Branch et al. 2008)).

We use all the *gold* SNe Ia with a phase of $-5 < p < 5$, because their S/N are high and they are easy to compare with previous measurements. The only exception is for “Si II λ 5454”, for which we restrict the analysis to the phase range $-5 < p < 3$, since this feature in the template spectra becomes unidentified at $p > 3$. The “Si II λ 5454” feature can be seen in almost all spectra with the phase $-5 < p < 5$. The unidentification of this feature in the template might be attributed to a bias in the training spectra for the template. In spite of several papers on the possibility of redshift evolution, few quantitative comparisons have been performed on a possible difference of distributions between samples of different redshift ranges for velocities and pEWs (Bronder et al. 2008).

An offset E to the temporal evolution of the Hsiao et al. (2007) template $X_p^{template}$ (and 1σ deviation, σ) was estimated by expanding error bars on each trend until a fit to produce a $\chi^2/\text{d.o.f.} = \frac{1}{N-1} \sum (X_p - (\bar{X}_p^{template} + E))^2 / (\sigma_p^2 + \sigma^2)$ of 1.0, where each SN measurement was (X_p, σ_p) . σ was assumed to be constant with phase so that the dispersions do not represent differences in observed numbers in each phase. The temporal evolution of the Hsiao et al. (2007) template shifted to represent the nearby SNe are shown as solid black lines in Figures 5 to 7, with dotted lines for their 1σ regions. Figures 8 and 9 are velocities/wavelengths and pEWs as a function of redshift; “Ca II λ 3945”, “Si II λ 4130”, “Si II λ 5454”, “Si II λ 5640”, “Si II λ 5972” and “Si II λ 6355” for velocities, “UV2” for wavelengths and “Ca II λ 3945”, “Si II λ 4130”, “Mg II λ 4300”, “Fe II λ 4800”, “Si II W”, “Si II λ 5972” and “Si II λ 6355” for

pEWs. Overplotted are the measurements to individual high- z SNe Ia spectra of Garavini et al. (2007) (blue pluses) and Bronder et al. (2008) (green pluses) and composite spectra of Foley et al. (2008a) (cyan pluses) and Sullivan et al. (2009) (orange pluses).

Table 5 summarizes the nearby and intermediate redshift comparisons of velocities, and the “UV2” wavelengths and pEWs for each feature. Column 1 is the name of feature. The number of SNe Ia, mean values and dispersions for nearby SNe Ia are listed from columns 2 to 4. These parameters for intermediate redshift SNe Ia are from columns 5 to 7. Column 8 is the probability of the Fisher F test that nearby and intermediate redshift SNe Ia have the same dispersion. Column 9 is the probability of the Student t test that nearby and intermediate redshift SNe Ia have the same mean. Since probabilities of the same dispersions vary, we calculate the Student’s t value without assuming an equal variance between nearby and intermediate redshift samples. This table indicates that distributions for all the features of intermediate redshift SNe Ia are consistent with nearby SNe Ia counterparts. The features for which different origins may be suspected are the “S II λ 5640” velocity and the “Si II λ 5972” pEW. We will discuss these suspected features in §5.

5. Discussion

The temporal and redshift evolution of UV to optical features for intermediate redshift SNe Ia have been presented and compared with those of nearby SNe Ia counterparts. Statistical tests have been performed to investigate the possibility of a change in average properties (Table 5). All the features are consistent between nearby and intermediate redshift SNe Ia within 2σ except for the “S II λ 5640” velocity and the “Si II λ 5972” pEW. This suggests that line profiles of intermediate redshift SNe Ia are similar to their nearby counterparts. These findings support the picture that SNe Ia are a “standard” candle for the intermediate redshift range.

We now examine the three features, “S II λ 5640”, “Si II λ 5972” and “Mg II λ 4300”, which have the lowest probability of being drawn from identical populations in the low- z and intermediate redshift samples. The “S II λ 5640” feature is narrow and easily affected by sky noise. Once an uncertainty in the mean value is taken into account, the nearby and intermediate redshift distributions become consistent at a significance level comparable to the other features, the probability of belonging to the same distribution going up to 0.18. The redshift average of our sample is $z \sim 0.2$, at which the biggest atmospheric line tends to overlap the “Si II λ 5972” feature. Although we attempted to remove sky lines completely, the larger deviation for the mid- z sample might be due to under/over subtraction of the unpredictable nature of the time variation. If, however, large pEWs for intermediate redshift

SNe Ia are real, then SNe Ia with larger “Si II λ 5972” pEWs would be explained by cooler SNe Ia (Hachinger et al. 2008). The next lowest probability of belonging to the same distribution is for the “Mg II λ 4300” pEW: the average pEW of “Mg II λ 4300” for intermediate redshift SNe Ia is $96\text{\AA}/89\text{\AA} \sim 8\%$ larger than the nearby average with a 12 % probability. Travaglio et al. (2005) simulated the metallicity effect on the detailed nucleosynthetic yields and showed that Mg is more synthesized by low metallicity progenitors. Assuming that the Mg synthesis rate is proportional to the “Mg II λ 4300” pEW, an $\sim 8\%$ mass increase corresponds to a decrease of progenitor metallicity by $\sim 0.2 Z_{\odot}$ (Travaglio et al. 2005). This is comparable to the average decrease of metallicity between nearby and intermediate redshift galaxies (Rodrigues et al. 2008).

We found similar velocity distributions for all the features of intermediate redshift and nearby SNe Ia (Figure 5 and Table 5). This finding is consistent with Nordin et al. (2011). However, we do not find significant differences in pEWs of “Si II λ 4130” (called “f2” in their paper) and “Fe II λ 4800” (called “f4” in their paper). The intermediate redshift sample of Nordin et al. (2011) contains a larger fraction of SNe Ia with high stretch (Guy et al. (2005), equivalent to x_1) than their nearby sample. Note that SNe Ia with high stretch have larger “Si II λ 4130” pEWs (Arsenijevic et al. 2008; Nordin et al. 2011). They also noticed a pEW-deficit subsample containing several SNe that likely would have been identified as peculiar if observed locally with higher S/N, possibly explaining the systematic pEW differences. Our intermediate redshift sample has the average x_1 of -0.06 ± 1.13 for $-5 < p < 5$ and this value is comparable to our nearby sample (-0.10 ± 0.48) in the same phase range. Thus, the inconsistency for this feature can be explained by the sample difference.

Some features for intermediate redshift SNe Ia can be compared with high- z trends from previous studies (Blondin et al. 2006; Garavini et al. 2007; Bronder et al. 2008; Sullivan et al. 2009) in Figures 8 and 9. Since their spectra are not available to the public, we use values determined in their papers and treated them in the same manner as we did our sample. For each feature, a high- z sample used in a previous study with the largest dataset was compared with intermediate redshift SNe Ia. We found in general the high- z and intermediate redshift samples to be similar. The velocity distributions for “Ca II λ 3945”, “S II λ 5454”, “S II λ 5640”, and “Si II λ 6355” come from the same population with $> 19\%$ probability. The pEW distributions agree for “Ca II λ 3945”, “Si II λ 4130”, and “Fe II λ 4800” with $> 16\%$ probability. Also the mean “Fe II λ 4800” pEW at $z = 0.33$ (Foley et al. 2008a) is consistent with our distribution.

However, the behavior of the “Mg II λ 4300” pEW is hard to understand. Figure 10 is the histogram of the “Mg II λ 4300” pEW distribution along with previous measurements. Distributions for nearby and intermediate redshift SNe Ia are shown in black and red. The 1σ

pEW region for the Sullivan et al. (2009) high- z sample is shown by two black-dotted lines. Blue and green histograms are for high- z SNe Ia by Garavini et al. (2007) and Bronder et al. (2008). High- z distributions differ from intermediate redshift by more than 3σ : the pEW for the composite spectrum of Sullivan et al. (2009) ($\bar{z} = 0.48$) is lower than the intermediate redshift average. They interpreted this as a larger fraction of hotter SNe Ia in the high- z Universe. This interpretation explains the larger fraction of SNe Ia with wide lightcurves (Howell et al. 2007), however it does not explain the line profile of the “Fe II $\lambda 4800$ ” feature for high- z SNe Ia (Foley et al. 2008a). The average pEWs for the Garavini et al. (2007) or Bronder et al. (2008) samples are, on the other hand, higher than the intermediate redshift average. Due to the finding of Howell et al. (2007), lower “Mg II $\lambda 4300$ ” pEW can be interpreted as a difference in the progenitor abundance (Travaglio et al. 2005) rather than as a larger fraction of cooler SNe Ia.

A spectroscopic luminosity indicator calibrates the maximum luminosity from a spectroscopic observable as does a lightcurve width (e.g. Phillips 1993) or a color (e.g. Tripp 1998). A flux ratio and pEWs have been suggested as its candidate. Bailey et al. (2009) presented that the flux ratio is best correlated with maximum absolute magnitude is $F(6420\text{\AA})/F(4430\text{\AA})$. Several papers have introduced an pEW of the “Si II $\lambda 4130$ ” feature (Bronder et al. 2008), the “Si II $\lambda 5972$ ” feature (Hachinger et al. 2006) and the ratio of the “Si II $\lambda 5972$ ” pEW to the Si II $\lambda 6355$ pEW (Hachinger et al. 2006) as a spectroscopic luminosity indicator. Suitable indicators should have a large intrinsic dispersion and small amount of pEW change with phase. As has been shown in Figure 7, the “Si II $\lambda 4130$ ” pEW shows the highest ratio of the pEW dispersion around the mean, and the least temporal evolution during $-5 < p < +5$. Moreover, the “Si II $\lambda 4130$ ” pEW is redshifted to wavelength regions less affected by night sky at intermediate redshift and can be also observed in the optical spectrograph for SNe Ia at $z \lesssim 1.2$. It can be said that the “Si II $\lambda 4130$ ” pEW is the best suited as a luminosity indicator among optical Si II lines. An indication of maximum luminosity from pEWs will be discussed in Konishi et al. (2011c).

We measured line velocities and pEWs of nearby spectra as well as intermediate redshift spectra, but, we had to use values of line velocities and pEWs presented in papers for high- z SNe Ia. Since it is difficult to remove the contribution of the host galaxy’s light completely at high- z , an unknown systematic error might remain in measurements by different authors. An uniform method for galaxy subtraction and feature measurements would be desired to compare spectra in different redshifts, after spectra have been reduced by various methods optimized by their telescopes.

6. Conclusion

We have derived line velocities, peak wavelengths and pEWs of spectral features during $-10 < p < 40$ for 59 normal intermediate redshift SNe Ia. Additionally, we compared the line profiles around the date of maximum brightness with nearby SNe Ia counterparts. We conclude the following: line velocities and pEWs for intermediate redshift SNe Ia are consistent with their nearby counterparts within 2σ . This supports the picture that SNe Ia are a “standard” candle for the intermediate redshift range as has been shown between SNe Ia at nearby and high redshifts. Although the probability that the velocity of the “S II $\lambda 5640$ ” feature for intermediate redshift and nearby SNe Ia comes from the same population shows a low probability, these samples are consistent within their uncertainties. A hint of larger “Mg II $\lambda 4300$ ” pEW distribution for intermediate redshift than nearby SNe Ia could be interpreted as the difference in the progenitor abundance.

Acknowledgements – We thank Harold Spinka for his careful reading of the manuscript for publication. K.K. thanks the COE Program “the Quantum Extreme Systems and Their Symmetries” for fiscal 2007, the Global COE Program “the Physical Sciences Frontier” for fiscal 2008, MEXT, Japan and the JASSO scholarship for fiscal 2007-2009. L.Ö is partially supported by the Spanish Ministry of Science and Innovation (MICINN) through the Consolidator Ingenio-2010 program, under project CSD2007-00060 “Physics of the Accelerating Universe (PAU)”.

Funding for the SDSS and SDSS-II was provided by the Alfred P. Sloan Foundation, the Participating Institutions, the National Science Foundation, the U.S. Department of Energy, the National Aeronautics and Space Administration, the Japanese Monbukagakusho, the Max Planck Society, and the Higher Education Funding Council for England. The SDSS Web site is <http://www.sdss.org/>.

The SDSS is managed by the Astrophysical Research Consortium (ARC) for the Participating Institutions. The Participating Institutions are The University of Chicago, Fermilab, the Institute for Advanced Study, the Japan Participation Group, The Johns Hopkins University, Los Alamos National Laboratory, the Max-Planck-Institute for Astronomy (MPIA), the Max-Planck-Institute for Astrophysics (MPA), New Mexico State University, University of Pittsburgh, Princeton University, the United States Naval Observatory, and the University of Washington. This research has made use of the NASA/IPAC Extragalactic Database (NED) which is operated by the Jet Propulsion Laboratory, California Institute of Technology, under contract with the National Aeronautics and Space Administration. Facilities: SDSS, Subaru(FOCAS)

REFERENCES

- Arsenijevic, V., Fabbro, S., Mourao, A.M., & Rica da Silva, A.J. 2008, *A&A*, 492, 535
- Altavilla, G., et al. *MNRAS*, 349, 1344
- Anupama, G.C., Sahu, D.K. & Jose, J. 2005, *A&A*, 429, 667
- Astier, P., et al. 2006, *A&A*, 447, 31
- Bailey, S., et al. 2009, *A&A*, 500, 17
- Baumont, S., et al. 2008, *A&A*, 491, 567
- Blondin, S., Walsh, J.R., Leibundgut, B., & Sainton, G. 2005, *A&A*, 431, 757
- Blondin, S., et al. 2006, *AJ*, 131, 1648
- Branch, D., 1981, *ApJ*, 248, 1076
- Branch, D., Drucker, W., & Jeffery, D.J. 1988, *ApJ*, 330, 117L
- Branch, D., Baron, E., Hall, N., Melakayil, M., & Parrent, J. 2005, *PASP*, 117, 545
- Branch, D., et al. 2008, *PASP*, 120, 135
- Bronder, T. J., et al. 2008, *A&A*, 477, 717
- Buta, R.J. & Turner, A. 1983, *PASP*, 95, 72
- Buta, R.J., Corwin Jr, H.C., & Opal, C.B. 1985, *PASP*, 97, 229
- Cardelli, J.A., Clayton, G.C., & Mathis, J.S. 1989, *ApJ*, 345, 245
- Ciatti, F., Barbon, R., Cappellaro, E., Rosino, L. 1988, *A&A*, 202, 15
- Coil, A.L., et al. 2000, *ApJ*, 544, L111
- Ellis, R.S., et al. 2008, *ApJ*, 674, 51
- Folatelli, G. 2004, *New A Rev.*, 48, 623
- Foley, R.J., et al., 2008, *ApJ*, 684, 68
- Foley, R.J., Filippenko, A.V., & Jha, S.W. 2008, *ApJ*, 686, 117
- Foley, R.J., et al. 2010, arXiv: 1010.2749

- Ford, C.H., Herbst, W., Richmond, M.W., Baker, M.L., Filippenko, A.V., Treffers, R.R., Paik, Y., & Benson, P.J. 1993, *AJ*, 106, 1101
- Frieman, J.A., et al. 2008, *AJ*, 135, 338
- Fukugita, M., et al. 1996, *AJ*, 111, 4
- Garavini, G., et al. 2007, *A&A*, 470, 411
- Gunn, J. E., et al. 1998, *AJ*, 116, 3040
- Gunn, J. E., et al. 2006, *AJ*, 131, 2332
- Guy, J., et al. 2005, *A&A*, 443, 781
- Guy, J., et al. 2007, *A&A*, 466, 11
- Hachinger, S., Mazzali, P. A., & Benetti, S. 2006, *MNRAS*, 370, 299
- Hachinger, S., Mazzali, P.A., Tanaka, M., Hillebrandt, W., & Benetti, S., 2008, *MNRAS*, 389, 1087
- Hamuy, M., Phillips, M.M., Maza, J., Wischnjewsky, M., Uomoto, A., Landolt, A.U., & Khatwani, R. 1991, 102, 208
- Holtzman, J.A., et al. 2008, *AJ*, 136, 2306
- Höflich, P., Wheeler, J. C., & Thielemann, F. K. 1998, *ApJ*, 495, 617
- Howell, D.A., Sullivan, M., Conley, A., & Carlberg, R., 2007, *ApJ*, 667, L37
- Hsiao, E. Y., Conley, A., Howell, D. A., Sullivan, M., Pritchett, C. J., Carlberg, R. G., Nugent, P. E., & Phillips, M. M. 2007, *ApJ*, 663, 1187
- Jha, S., et al. 1999, *ApJS*, 125, 73
- Kashikawa, N., et al. 2002, *PASJ*, 54, 819
- Kessler, R., et al. 2009, *ApJS*, 185, 32.
- Konishi, K., et al. 2011a, arXiv: 1101.1565
- Konishi, K., et al. 2011c, in prep
- Krisciunas, K., et al. 2001, *AJ*, 122, 1616

- Krisciunas, K., et al. 2003, AJ, 125, 166
- Krisciunas, K., et al. 2004, AJ, 127, 1664
- Leibutgut, B., et al. 1993, AJ, 105, 301
- Lentz, E. J., Baron, E., Branch, D., Hauschildt, P. H., & Nugent, P. E. 2000, ApJ, 530, 966
- Li, W., Filippenko, A. V., Gates, E., et al. 2001, PASP, 113, 1178
- Lira P. et al., 1998, AJ, 115, 234
- Mannucci, F., Della Valle, M., & Panagia, N., 2006, MNRAS, 370, 773
- Matheson, T., et al. 2008, ApJ, 135, 1598
- Miknaitis, G., et al. 2007, ApJ, 666, 674
- Nordin et al. 2011, A&A, 526, 119
- Nomoto, K., Thielemann, F.-K., & Yokoi, K. 1984, ApJ, 286, 644
- Nugent, P., Kim, A., & Perlmutter, S. 2002, PASP, 114, 803
- Oke, J.B., et al. 1995, PASP, 107, 375
- Östman, L. et al., 2011, A&A, 526, A28
- Perlmutter, S., 1999, ApJ, 517, 565
- Phillips, M.M., et al. 1987, PASP, 99, 592
- Phillips, M.M. 1993, ApJ, 413, L105
- Phillips, M.M., Lira, P., Suntzeff, N.B., Schommer, R.A., Hamuy, M. & Maza, J. 1999, AJ, 118, 1766
- Riess, A.G., Press, W.H. & Kirshner, R.P. 1996, ApJ, 473, 88
- Riess, A. G., et al. 1998, AJ, 116, 1009
- Riess, A. G., et al. 1999, AJ, 117, 707
- Riess A. G. et al., 2005, ApJ, 627, 579
- Sako, M., et al. 2008, AJ, 135, 348

- Rodrigues, M., et al. 2008, A&A, 492, 371
- Schlegel, D.J., Finkbeiner, D.P. & Davis, M 1998, ApJ, 500, 525
- Stehle, M., Mazzali, P.A., Benetti, S., & Hillebrandt, W. 2005, MNRAS, 360, 1231
- Stoughton, C., et al., 2002, AJ, 123, 485
- Sullivan, M., Ellis, R.S., Howell, D.A., Riess, A., Nugent, P.E. & Gal-Yam, A. ApJ, 693, 2009
- Travaglio, C., Hillebrandt, W., & Reinecke, M. 2005, A&A, 443, 1007
- Tripp, R., 1998, A&A, 331, 815
- Valentini, G., et al. 2003, ApJ, 595, 779
- York., D.G., et al. 2000, AJ, 120, 1579
- Weiler, K.W. 2003, Supernovae and Gamma-Ray Bursters (Springer)
- Wells, L.A., et al. 1994, AJ, 108, 2233
- Zheng, C., et al. 2008, AJ, 135, 1766

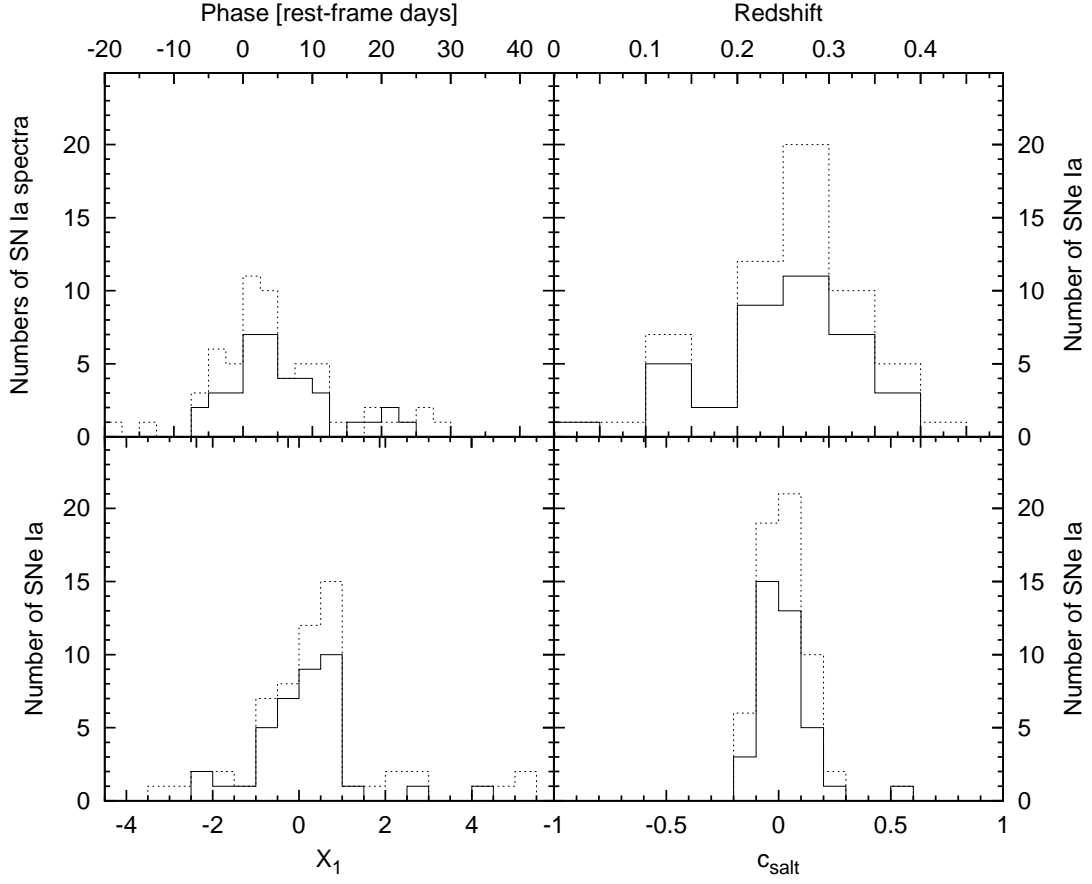


Fig. 1.—: Distributions of SN phase (top left), redshift (top right), lightcurve width x_1 (bottom left) and color c_{salt} (bottom right) for the intermediate redshift sample; total of 59 SNe Ia (dotted) and 38 *gold* SNe Ia (solid).

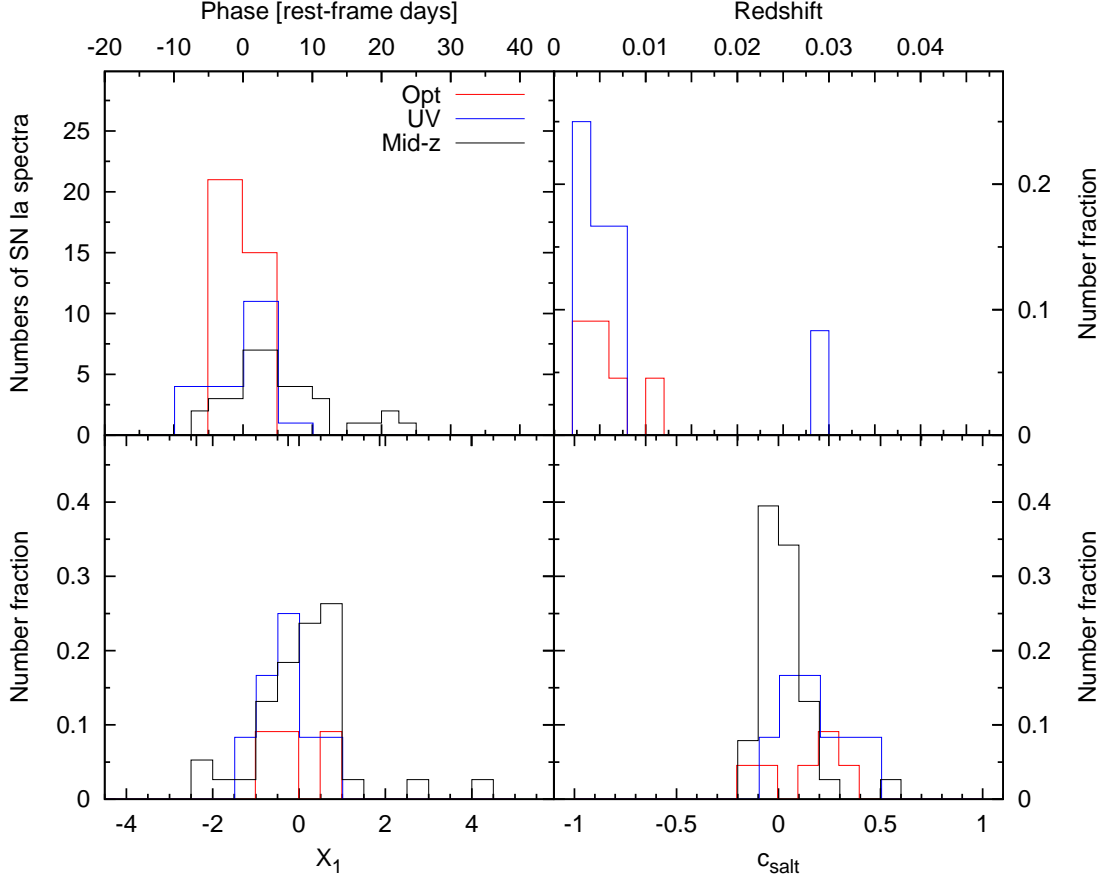


Fig. 2.—: Distributions of SN phase (top left), redshift (top right), lightcurve width x_1 (bottom left) and color c_{salt} (bottom right) for two control samples, the **Opt** (red) and **UV** (blue) and 38 intermediate redshift *gold* sample (black) for a reference. The histograms for redshift, lightcurve width x_1 and color c_{salt} are normalized so that the area under the intermediate redshift sample is the same as for the reference samples.

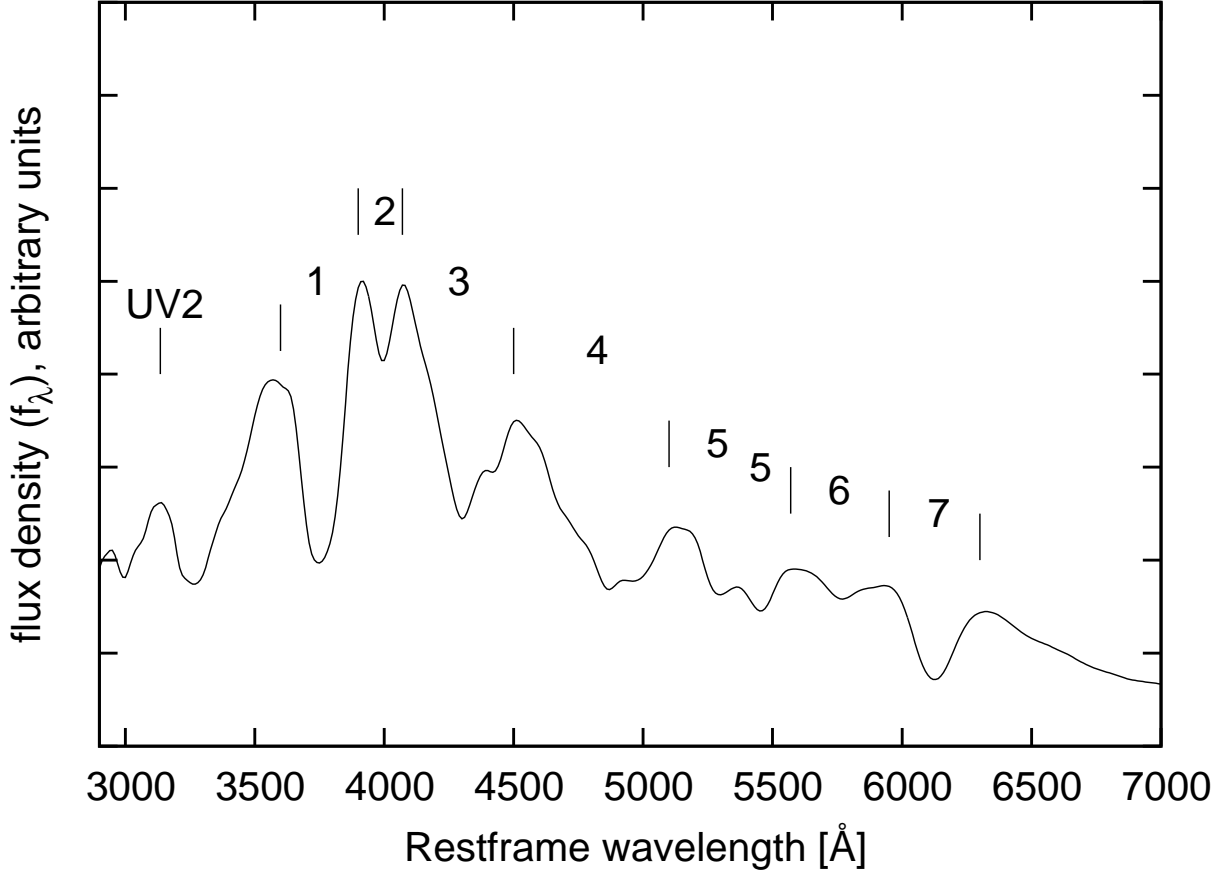


Fig. 3.—: SN Ia spectral feature definitions at near maximum brightness: Labels correspond to the following feature names: UV2- "UV2", 1- "Ca II λ 3945", 2- "Si II λ 4130", 3- "Mg II λ 4300", 4- "Fe II λ 4800", 5- "S II λ 5454" and "S II λ 5640", 6- "Si II λ 5972" and 7- "Si II λ 6355". See also Table 4. The wavelengths of absorption lines are shifted blueward due to the expansion of SN ejecta. Differences of absorption minima from their nominal wavelengths (line velocities) have been measured as described in §3.2.

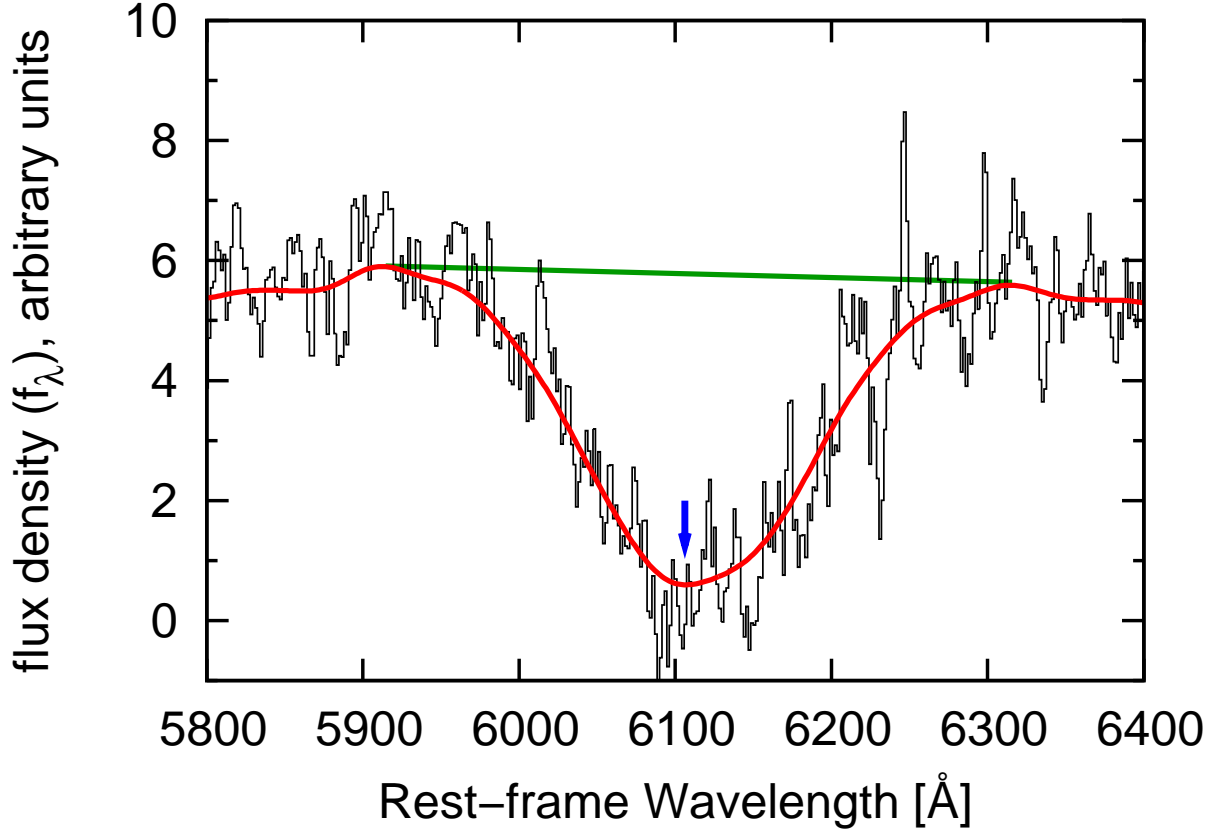


Fig. 4.—: An example of velocity and pEW measurements. The black histogram is the un-smoothed Subaru spectrum taken near the maximum brightness (SN16776). The smoothed spectrum is shown in the red curve. The pseudo continuum is determined for the "Si II λ 6355" feature (green line). The absorption minimum wavelength (vertical arrow) in the smoothed spectrum is used to determine an absorption minimum and absorption boundaries for an pEW measurement.

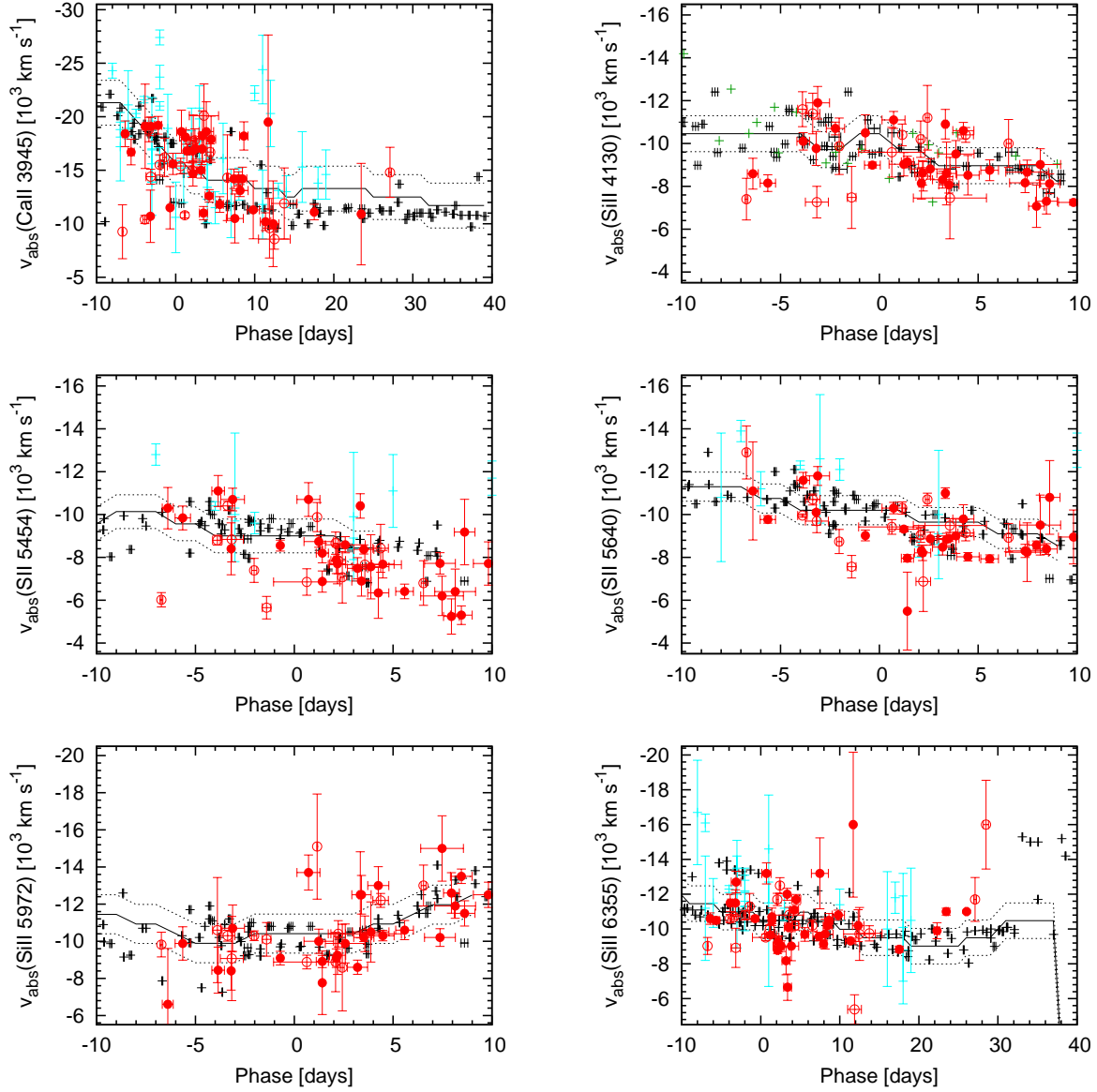


Fig. 5.—: The temporal evolution of absorption line velocities for various features; phases are rest-frame days. The intermediate redshift sample is shown as red circles (filled circles for the *gold* sample and open circles for the *silver* sample. Details are described in §4.1). The **Opt** sample is given as black pluses. Overplotted are the results of Blondin et al. (2006) (cyan pluses) and Ellis et al. (2008) (green pluses). The measurements for the Hsiao et al. (2007) template shifted to represent the nearby mean trend are shown as the solid line. Two dotted lines are $\pm 1\sigma$ of the intermediate redshift sample.

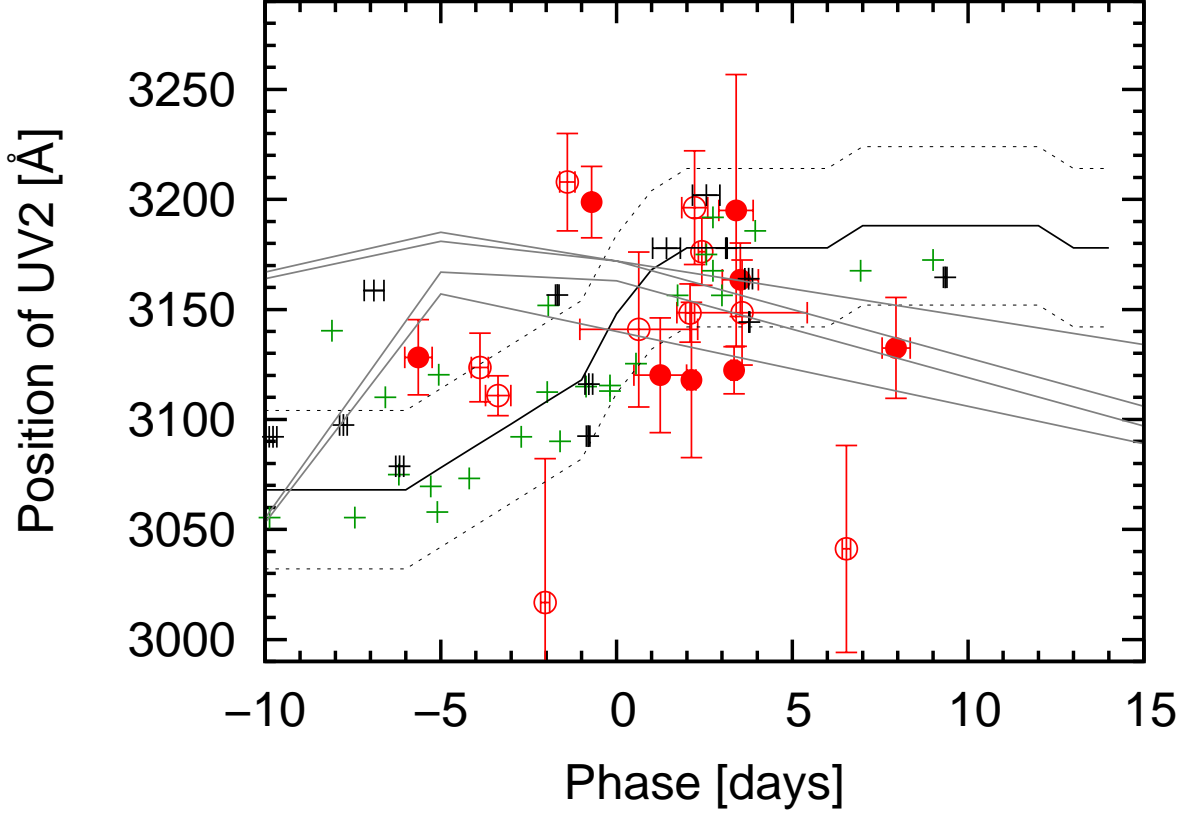


Fig. 6.—: Peak wavelengths for the “UV2” feature plotted versus rest-frame phase for the Subaru data (red circles) and the **UV** sample (black pluses). Overplotted are the results of Ellis et al. (2008) (green pluses). The four gray lines represent the results of theoretical templates of Lentz et al. (2000) for the different metallicities in the unburned CO layer (top to bottom: 0.1, 0.3, 1.0 and 3.0 times solar metallicity). The measurements for the Hsiao et al. (2007) template shifted to represent the nearby mean trend are shown as the solid black line. Two dotted lines are $\pm 1\sigma$ of the intermediate redshift sample.

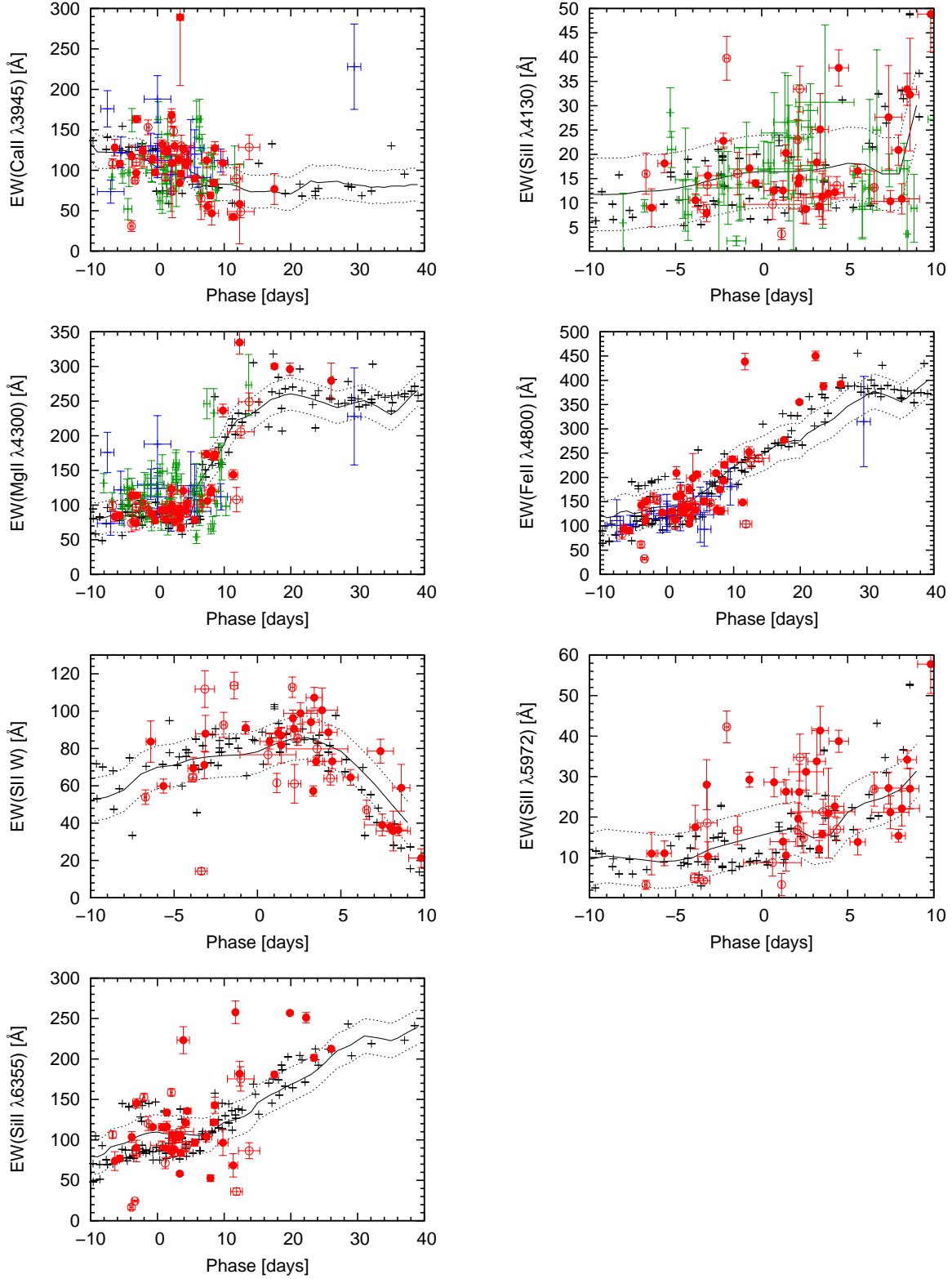


Fig. 7.—: The temporal evolution of equivalent widths for various elements. The symbols are the same as in Figure 5. The SCP SNe Ia (Garavini et al. 2007) are marked in blue and the SNLS SNe Ia (Bronder et al. 2008) are marked in green.

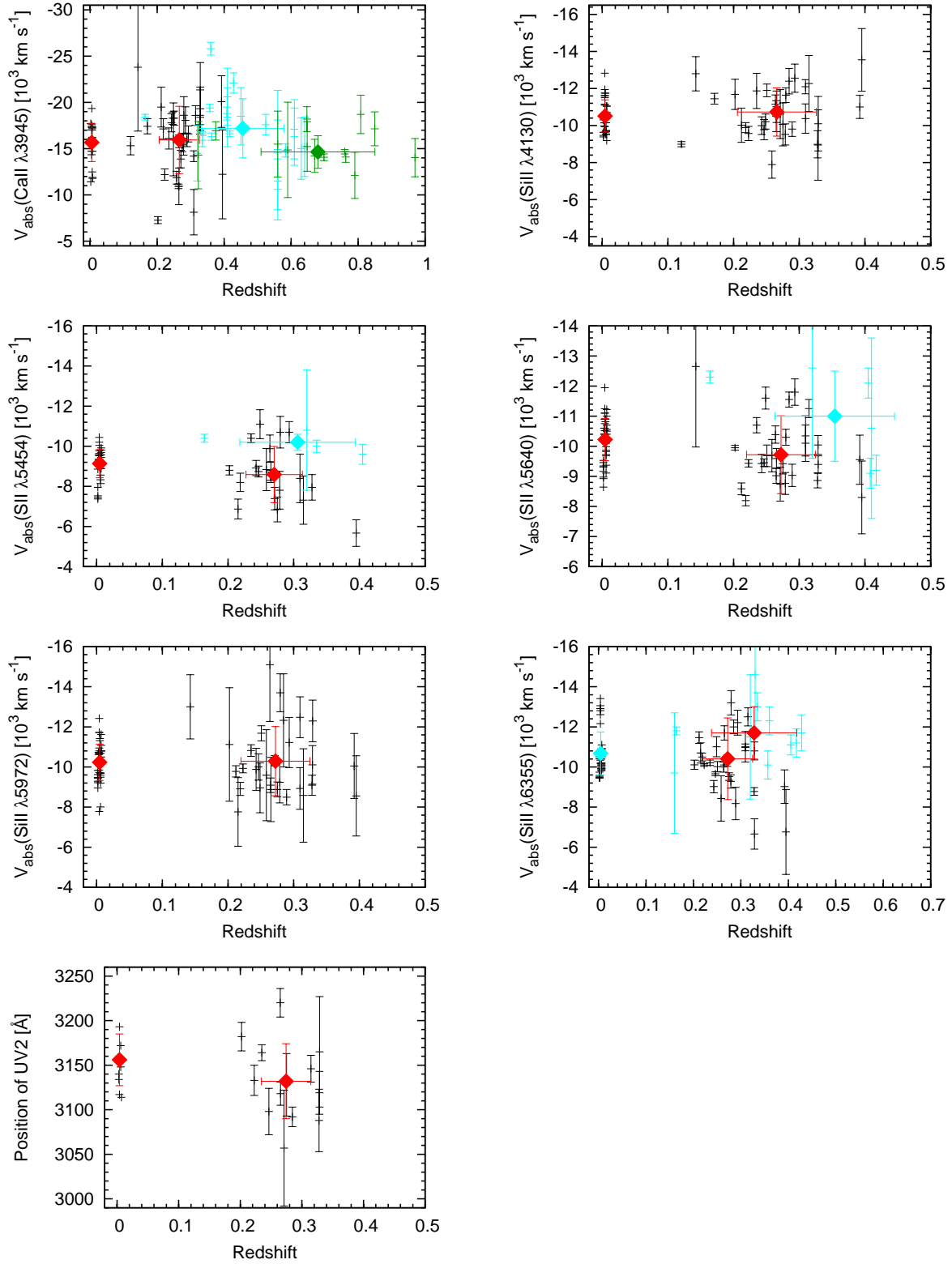


Fig. 8.—: Phase-corrected absorption line velocities as a function of redshift for various elements for nearby and intermediate redshift (black) and high- z SNe Ia (cyan and green). Two big red diamonds are averages and standard deviations of nearby and intermediate redshift samples. (see also text)

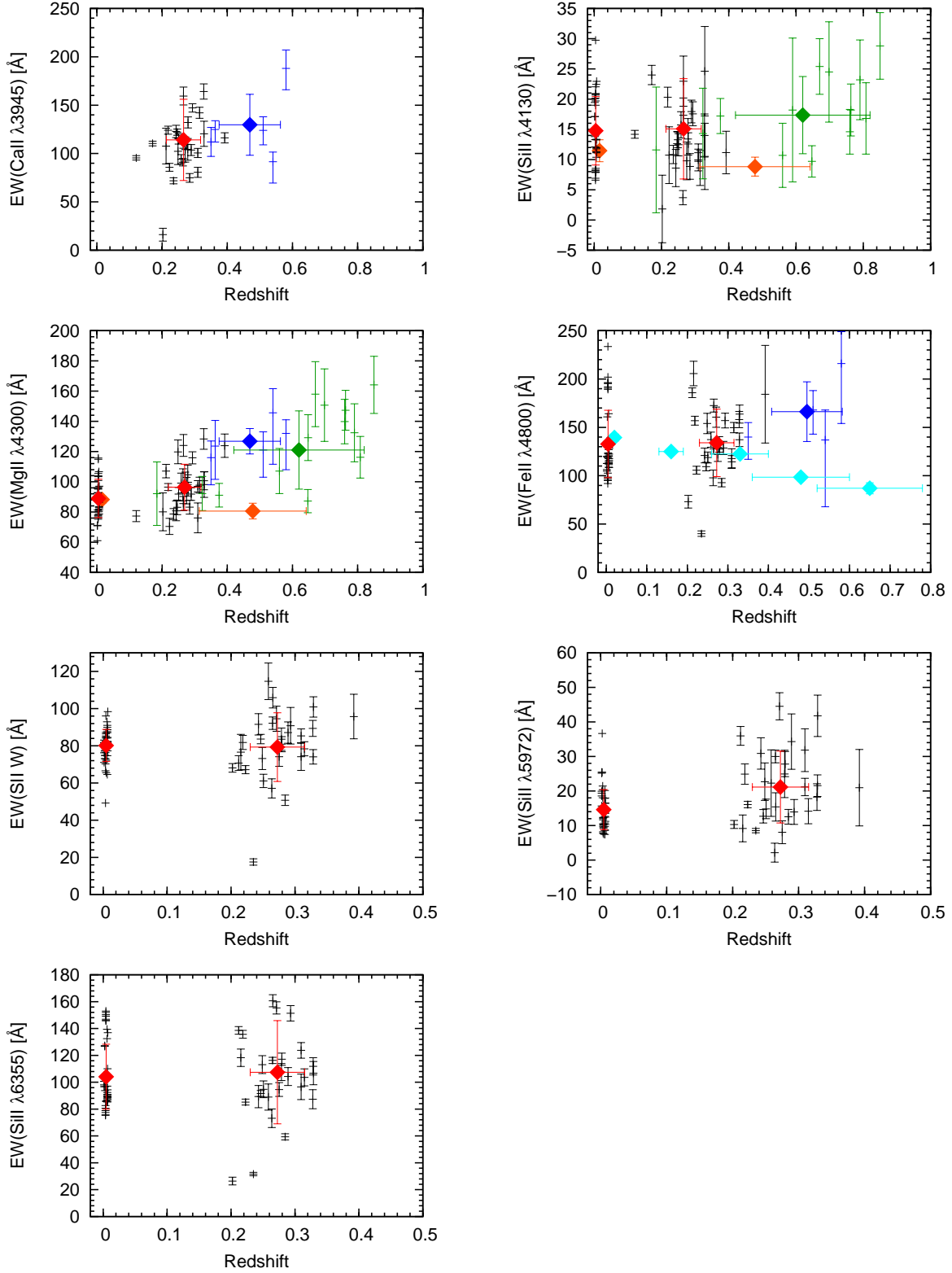


Fig. 9.—: Phase-corrected equivalent widths as a function of redshift for various elements for nearby and intermediate redshift (black) and high-z SNe Ia (cyan, blue, green). Two big red diamonds are averages and standard deviations of nearby and intermediate redshift samples. (see also text)

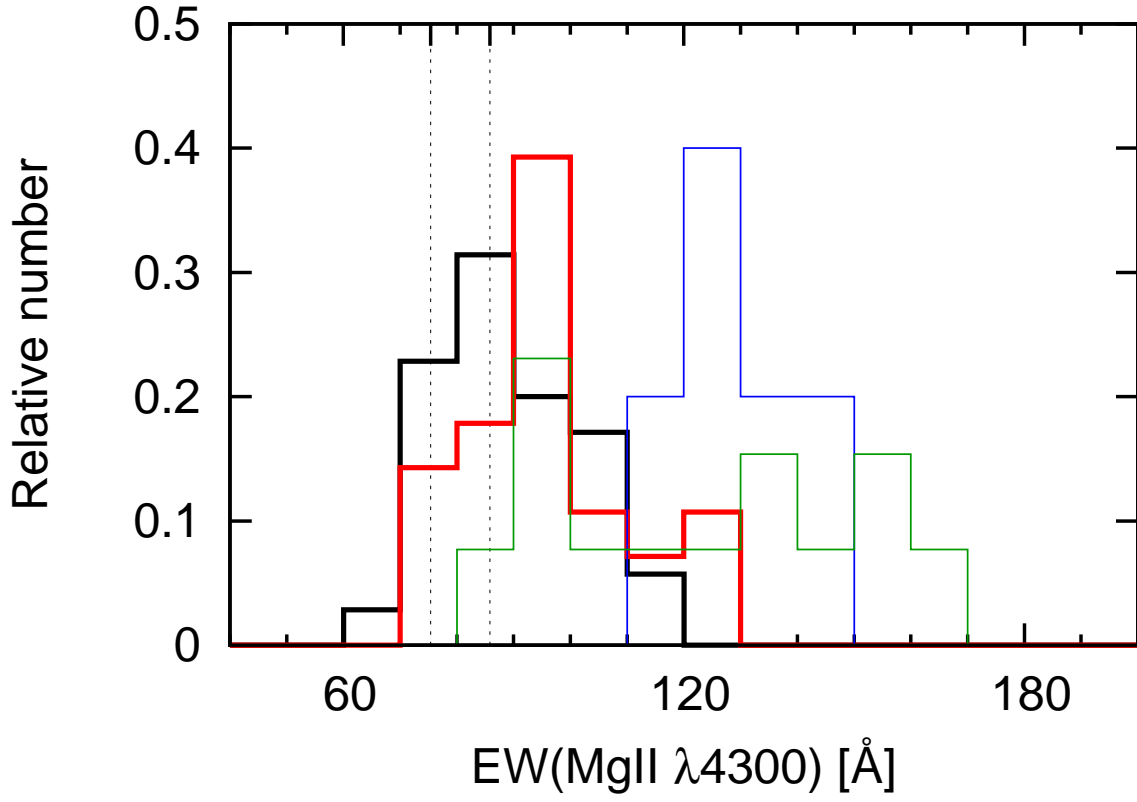


Fig. 10.—: Histograms of phase-corrected equivalent widths for the “MgII $\lambda 4300$ ” feature: nearby (black) and intermediate redshift sample (red). The 1σ pEW region for the Sullivan et al. (2009) high- z sample is shown by two black-dotted lines. Blue and green histograms are for the Garavini et al. (2007) and Bronder et al. (2008) high- z samples.

Table 1. Normal Type Ia Supernovae observed by Subaru/FOCAS

SDSS ID	IAU name ^a	$E(B - V)_{MW}$ ^b	MJD ^c	Redshift ^d	Sample ^e	SN phase ^f
1119	2005fc	0.060	53640.26	0.2974 (ge)	PS	12.5
1166	–	0.019	53641.39	0.3814 (ga)	G	7.5
1686	–	0.055	53640.42	0.1362 (ge)	G	11.7
1688	–	0.050	53641.25	0.3591 (ge)	G	8.1
2165	2005fr	0.033	53641.42	0.2841 (sn)	G	5.6
2330	2005fp	0.024	53641.35	0.2129 (ge)	G	4.5
2422	2005fi	0.039	53641.32	0.2628 (ge)	SS	1.2
2635	2005fw	0.096	53670.60	0.1434 (ge)	G	23.5
2789	2005fx	0.051	53640.38	0.2862 (ga)	G	3.2
2992	2005gp	0.087	53669.63	0.1261 (ge)	G	22.3
3080	2005ga	0.048	53670.36	0.1743 (ge)	G	17.5
3451	2005gf	0.056	53640.31	0.2497 (ge)	G	-3.8
3452	2005gg	0.059	53640.34	0.2311 (ge)	G	-6.4
5391	2005hs	0.111	53669.56	0.3003 (ge)	G	8.6
5533	2005hu	0.070	53669.25	0.2199 (ge)	G	1.4
5717	2005ia	0.031	53670.28	0.2521 (ge)	SS	4.4
5737	2005ib	0.038	53670.32	0.3933 (ge)	G	3.9
5751	2005hz	0.022	53701.33	0.1308 (ge)	SS	27.1
5844	2005ic	0.121	53669.29	0.3120 (ge)	G	4.3
5944	2005hc	0.030	53701.49	0.0445 (ge)	G	26.0
5957	2005ie	0.036	53669.60	0.2796 (ge)	G	2.2
6057	2005if	0.119	53700.54	0.0669 (ge)	SS	28.5
6108	2005ih	0.054	53671.33	0.2599 (ge)	SS	-3.2
6196	2005ig	0.063	53670.25	0.2811 (ga)	G	0.7
6249	2005ii	0.041	53671.39	0.2947 (ge)	G	-3.1
6406	2005ij	0.081	53700.50	0.1244 (ge)	G	19.9
6699	2005ik	0.053	53671.29	0.3105 (ge)	G	-3.2
9032	2005le	0.060	53700.23	0.2541 (ge)	G	8.5
9207	2005lg	0.038	53700.47	0.3496 (ge)	G	9.8
10449	2005ll	0.062	53701.23	0.2415 (ge)	G	2.6
10550	2005lf	0.036	53700.30	0.3000 (ge)	G	7.4
12855	2006fk	0.052	53993.27	0.1722 (ga)	G	-2.2
12860	2006fc	0.069	53993.28	0.1210 (ge)	G	-0.3
12869	2006ge	0.140	53996.24	0.2841 (ge)	PS	13.7
12883	2006fr	0.102	53995.30	0.3060 (ge)	SS	11.9
12972	2006ft	0.023	53995.43	0.2606 (ge)	G	11.4
12977	2006gh	0.025	53996.50	0.2474 (ge)	G	1.2
13025	2006fx	0.083	53995.35	0.2240 (ge)	G	3.5
13099	2006gb	0.039	53995.39	0.2655 (ge)	G	-0.7
13152	2006gg	0.021	53996.40	0.2031 (ge)	SS	-3.9
13174	2006ga	0.026	53995.48	0.2357 (ge)	SS	-3.4
13327	2006jf	0.057	53996.32	0.2814 (ge)	PS	-21.5
13934	2006jg	0.102	54023.41	0.3310 (ge)	G	12.3
14261	2006jk	0.094	54023.27	0.2853 (ge)	G	3.3
14298	2006jj	0.076	54023.23	0.2692 (sn)	G	8.0
14456	2006jm	0.090	54023.46	0.3283 (ge)	G	3.4

Table 1—Continued

SDSS ID	IAU name ^a	$E(B - V)_{MW}$ ^b	MJD ^c	Redshift ^d	Sample ^e	SN phase ^f
15217	2006jv	0.029	54023.49	0.371 (sn)	PS	-1.4
15219	2006ka	0.037	54023.54	0.2467 (ge)	G	-5.6
16631	2006pv	0.128	54065.53	0.207 (sn)	G	1.4
16758	2006pw	0.085	54065.25	0.3261 (ge)	PS	2.4
16776	2006qd	0.044	54066.30	0.2667 (ge)	PS	2.1
16779	2006qa	0.105	54065.44	0.3983 (ge)	SS	6.5
16781	2006qb	0.111	54065.48	0.3257 (ge)	PS	3.6
16847	2006px	0.033	54066.30	0.2767 (ge)	PS	0.6
16938	2006qe	0.047	54065.29	0.386 (sn)	S	2.2
16953	2006pp	0.024	54065.33	0.3387 (ge)	G	2.1
17048	2006qi	0.025	54065.36	0.189 (sn)	S	-6.7
17081	2006ql	0.038	54065.40	0.2749 (ga)	PS	-2.0
17117	2006qm	0.032	54066.38	0.1404 (ge)	PS	-12.6

^aIAU names were not attached to three SNe due to on-site analysis.

^bColor excess within our Galaxy.

^cThe observational mid-date. The red part of a spectrum is first observed and the blue part follows.

^dHeliocentric redshift. “ge” indicates that the redshift of the target was determined from galaxy emission line(s), “ga” from galaxy absorption line(s) and “sn” for redshift from SN spectrum fitting.

^eThe validity of the data; G: *gold* sample, PS: *silver* lightcurves, SS: *silver* spectrum, S: *silver* lightcurves & spectrum

^fThe SN phase is the rest-frame phase in days from their maximum brightness date.

Table 2. Type Ia Supernovae in the **Opt** sample

IAU Name	RA	Dec	$E(B - V)_{MW}$ ^a	z_{spec}
1981B	188.62	2.20	0.013	0.0060
1989B	170.06	13.01	0.013	0.0024
1990N	190.74	13.26	0.018	0.0034
1991M	239.65	17.46	0.030	0.0072
1994D	187.87	7.98	0.013	0.0015
1996X	199.50	-26.85	0.068	0.0069
1998aq	179.11	55.13	0.014	0.0037
1998bu	169.69	11.84	0.025	0.0030
1999ee	334.04	-36.84	0.059	0.0114
2000E	309.31	66.10	0.371	0.0047
2002bo	154.53	21.83	0.051	0.0042
2003du	218.65	59.33	0.010	0.0064

Note. — RA and Dec in Column 2 and 3 are the Right Ascension and Declination (J2000) in degrees.

^aColor excess within our Galaxy.

Table 3. Type Ia Supernovae in the **UV** sample

IAU Name	RA	Dec	$E(B - V)_{MW}$ ^a	z_{spec}
1980N	50.75	-37.21	0.046	0.0059
1981B	188.62	2.20	0.013	0.0060
1982B	108.64	84.39	0.064	0.0074
1983G	193.09	-1.20	0.010	0.0041
1989B	170.06	13.01	0.013	0.0024
1990N	190.74	13.26	0.018	0.0034
2001ba	174.51	-32.33	0.060	0.0296
2001el	56.13	-44.64	0.094	0.0039

Note. — RA and Dec in Column 2 and 3 are the Right Ascension and Declination (J2000) in degrees.

^aColor excess within our Galaxy.

Table 4. Line measurements

Feature ID	Label	Wavelength ranges ^a Absorption minimum	Absorption boundaries (blue, red)	Rest Wavelength [Å] ^b
UV2	“UV2”	3050:3200	-, -	-
1	“Ca II λ 3945”	3650(3700):4000	3500(4000 ^c):3720, 3860:4050	3945
2	“Si II λ 4130”	3950:4100	3860:4000, 4000:4220	4130
3	“Mg II λ 4300”	-	3900(4000 ^d):4150, 4450:4700	-
4	“Fe II λ 4800”	-	4450:4700, 5050:5590	-
5	“S II W”	5240:5365, 5400:5545	5080:5400, 5500:5700	5454, 5640
6	“Si II λ 5972”	5650:5850	5550:5700, 5800:6000	5972
7	“Si II λ 6355”	5900:6300	5820:6000, 6200:6540(6400 ^e)	6355

^aWe select different search wavelength ranges from Garavini et al. (2007) to optimize for automated measurements of our dataset. A wavelength of an absorption minimum or a blue/red absorption boundary is measured within the range of λ_a and λ_b for $\lambda_a : \lambda_b$.

^bThe rest-frame wavelengths for the transition of the given ion; the weighted mean wavelength of the two strongest transitions for ID1 and ID7, and the wavelength of the strongest transition for ID2, ID5 and ID6 (Blondin et al. 2006).

^cFor the phase range of $-10.0 \leq p < +0.0$.

^dFor the phase range of $-10.0 \leq p < +6.5$. The “Si II λ 4130” feature gets merged to “Mg II λ 4300” at $p > 6.5$.

^eFor the phase range of $-10.0 \leq p < +5.0$.

Table 5. The nearby and intermediate redshift comparisons for each feature

Features	Nearby			Mid-z			P(F test) ^a	P(T test) ^b
	N	mean	deviation	N	mean	deviation		
Velocity ^c								
Ca II λ 3945	23	-15.7	21.0	19	-16.2	23.5	0.61	0.44
Si II λ 4130	34	-10.5	8.6	19	-10.5	9.2	0.72	0.79
S II λ 5454	38	-9.1	6.9	11	-8.9	11.7	0.02	0.53
S II λ 5640	46	-10.2	6.8	18	-9.6	11.0	0.02	0.05 ^e
Si II λ 5972	45	-10.2	8.9	18	-10.0	11.9	0.12	0.39
Si II λ 6355	47	-10.7	10.6	18	-10.3	14.4	0.10	0.26
Wavelength ^d								
UV2	8	3146	32	6	3147	32	0.92	0.18
Equivalent width ^d								
Ca II λ 3945	16	103	23	19	112	24	0.88	0.27
Si II λ 4130	35	15	6	19	16	6	0.97	0.56
Mg II λ 4300	35	89	13	18	96	16	0.30	0.12
Fe II λ 4800	44	133	24	18	138	24	0.95	0.46
S II W	47	80	9	18	81	11	0.28	0.73
Si II λ 5972	46	15	6	18	23	8	0.13	<0.01
Si II λ 6355	46	104	24	18	113	24	0.95	0.19

^aA probability that nearby and intermediate redshift SNe Ia have the same dispersion.

^bA probability that nearby and intermediate redshift SNe Ia have the same mean.

^cValues in column 3, 4, 6, 7 are velocities in units of 10^3 km sec^{-1} . The mean values in columns 3 and 6 are offsets from the trends of the Hsiao et al. (2007) template spectra.

^dValues in column 3, 4, 6, 7 are wavelengths or EWs in units of Å. The mean values in columns 3 and 6 are offsets from the trends of the Hsiao et al. (2007) template spectra.

^eThe probability from the same distribution going up to 0.18, when an uncertainty on the mean value is taken into account.